The Interplay of Nonlinearity and Architecture in Equilibrium Cytoskeletal Mechanics

Shenshen Wang,[1] Tongye Shen,[2] and Peter G. Wolynes[1]

[1]*Department of Physics, Department of Chemistry and Biochemistry,*
and Center for Theoretical Biological Physics, University of California, San Diego, La Jolla, CA 92093, USA
[2]*Department of Biochemistry, Cellular and Molecular Biology,*
University of Tennessee, Knoxville, TN 37996, USA
(Dated: July 1, 2011)

The interplay between cytoskeletal architecture and the nonlinearity of the interactions due to bucklable filaments plays a key role in modulating the cell's mechanical stability and affecting its structural rearrangements. We study a model of cytoskeletal structure treating it as an amorphous network of hard centers rigidly cross-linked by nonlinear elastic strings, neglecting the effects of motorization. Using simulations along with a self-consistent phonon method, we show that this minimal model exhibits diverse thermodynamically stable mechanical phases that depend on excluded volume, crosslink concentration, filament length and stiffness. Within the framework set by the free energy functional formulation and making use of the random first order transition theory of structural glasses, we further estimate the characteristic densities for a kinetic glass transition to occur in this model system. Network connectivity strongly modulates the transition boundaries between various equilibrium phases, as well as the kinetic glass transition density.

I. INTRODUCTION

The cytoskeleton is a crowded network of dynamic filamentous protein polymers that collaborate with diverse binding proteins and molecular motors to form nature's most marvelous active material[1]. All eukaryotic cells are known to contain a well-developed cytoskeleton, and even bacteria have been found to contain a diverse set of proteins capable of forming structural filaments[2]. Actin is a major constituent of the cytoskeletal network that participates in such widely differing processes as blood clotting, egg fertilization, intestinal absorption and tumor invasion. A common theme of many substantial experimental efforts[3–7] is the role of actin filaments in maintaining cell architecture and generating movement.

In vitro, actin can polymerize to form long rigid filaments (F-actin), with a diameter around 7 nm and contour length up to 20 μm. The *in vivo* cytoskeletal network, however, is regulated and controlled not only by the concentration of F-actin, but also by accessory proteins that bind to F-actin. Nature provides a host of actin-binding proteins (ABPs) with versatile functions that offer the necessary variations for the part actin has to play[8]: Cross-linking proteins form filament bundles or isotropic gels, whereas capping proteins and/or filament-severing proteins regulate actin polymerization under specific salt conditions and thus control the average length of F-actin. Experiments show, for example, that actin-binding protein functions to stabilize cortical actin *in vivo* and is required for efficient cell locomotion[9]. Rheological experiments on simplified networks and living cells demonstrate that even the most basic mechanical properties of cytoskeletal materials are sensitive to specific architectural details, including filament and cross-link density, connectivity, and orientation[10].

Unlike flexible polymers, where changes in cross-link density typically do not markedly affect the elasticity, small changes in the concentration of cross-linking

actin-binding proteins do dramatically alter the elasticity of F-actin networks[11]. As materials, *in vitro* networks of cytoskeletal filaments exhibit several unusual mechanical properties, including a highly nonlinear elastic response[7,12] and negative normal stresses[13]. Another noteworthy observation is the buckling of actin stress fibers that occurs upon rapid shortening[14], which demonstrates the instability of a prestressed actin network under compression.

A refined experimental route to understanding cytoskeletal structures in terms of their molecular components is to reconstitute these structures from purified proteins. *In vitro* reconstitution provides the capability to study the emergence of micrometer-scale function from numerous molecular-scale interactions. A recent reconstitution of contractility in a simplified model system, composed of purified F-actin, muscle myosin II motors and α-actinin cross-linkers, has shown that contractility occurs above a threshold motor concentration (one myosin filament for every 30 actin filaments) and within a window of cross-link concentrations ($90-270$ α-actinin dimers per actin filament)[15]. It is somewhat unexpected that at high cross-link densities the bundled networks do not contract on the experimental timescale of an hour. This seems to imply a dramatic slow-down of cytoskeletal kinetics due to the steric constraints associated with increasing crowding.

The cytoskeleton in different organisms or even during different stages of the cell cycle exhibits a rich variety of viscoelastic properties[16,17]. To accommodate both the adaptive behavior of dynamic remodeling, and the ability to stabilize and be resistant to deformation, the cytoskeleton should exhibit at least two mechanical phases: a plastic/fluid phase for internal reorganization of the cell, and an elastic/solid phase for mechanical support and tension transmission.

In contrast to the strain-stiffening behavior[18] in response to a *sustained* stretching of cells or reconstituted

cross-linked actin gels, measurements on the responses to a *transient* stretching in the living cells[19] demonstrate that the cell will fluidize in response to the stretch, but will resolidify subsequent to this fluidization. This ability seems to be insensitive to molecular details, and instead only depends on the proximity of the thermodynamic conditions of the cell to a solid-like state before the stretch. This observation implied that in addition to specific signalling pathways, some response mechanisms are most likely controlled by non-specific actions of a slowly evolving network of physical forces. On the other hand, the universal behavior observed in the osmotically compressed cell[20] highlighted the crowding-induced stiffening of the cytoplasm as the solid volume fraction is sufficiently high, and suggested an analogy to the colloidal glass transition.

In an attempt to understand the interplay between the individual filament properties and network architecture, we study in this paper the equilibrium properties of a model cytoskeleton as an amorphous network of rigidly cross-linked nonlinear strings which also contains nodes with excluded volume. We incorporate the nonlinearity of interaction due to bucklable filaments into the force law, and characterize the cytoskeletal architecture by cross-link density and network connectivity. A mean-field level investigation, within the framework of the self-consistent phonon method and a density functional formulation, reveals a diversity of mechanical phases and a number of possible transitions in between which can be controlled by biophysical parameters. This phase diagram may shed light on our understanding of cytoskeletal remodeling in response to mechanical or chemical stimuli. We also show the possibility of a glass transition in this model system and how the network connectivity modulates the transition densities.

II. MODEL AND METHOD

A. Model

We model the F-actin bundles as individual nonlinear elastic strings; they are capable of resisting tensile forces by stretching (beyond the relaxed length L_e), but are unstable under compression so that these forces may cause the strings to buckle. The actin-binding proteins bundle and crosslink F-actin to form an amorphous network. To account for the excluded volume of F-actin and the ABP aggregates, to the lowest order, we model the network as being crosslinked by hard "beads"; each bead serves as a compact rigid subunit that concentrates the volume of the F-actin and ABP aggregates centered on that bead. The network elasticity then comes from the remaining inter-bead F-actin molecules which are now taken to be volumeless. To higher order, the elasticity within the beads can also be included by introducing softness in the repulsion. In this way we effectively decompose the inter-bead interaction into purely excluded volume and

nonlinear elastic contributions, and the model potential energy $V(r)$ between a nearest-neighbor pair of beads is given by

$$\beta V(r) = A\,\Theta(d-r) + \frac{\beta\gamma}{2}(r - L_e)^2\,\Theta(r - L_e)\,, \quad (1)$$

where $\Theta(x)$ is the Heaviside step function. The limit $A \to \infty$ indicates the hard-sphere (HS) repulsion, while γ measures the rigidity of the inter-bead F-actin. Temperature dependence enters this model only via the combination $\beta\gamma$ where $\beta = 1/k_B T$. Here d denotes the HS diameter of the beads and L_e marks the onset of elasticity. Thus $L_e > d$ define a buckling regime ($d < r < L_e$) where no load is imposed. We show a sketch of the model system (Fig. 1a) and a schematic of the nonlinear interaction (Fig. 1b).
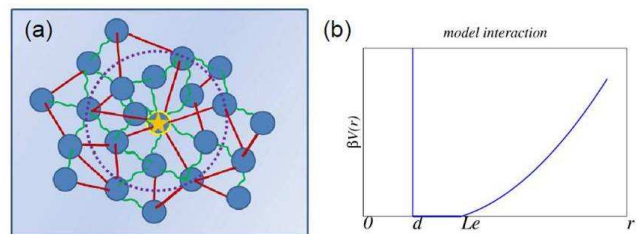

FIG. 1: Illustrations of the model system and the nonlinear interaction. (a) The beads (blue spheres) interconnect the F-actin (red straight or green squiggly lines) into an amorphous network. Red straight lines stand for tense/stretched bonds and green squiggly lines for loose/buckled bonds. The arbitrarily chosen central particle (yellow-stared) is connected with its nearest neighbors within the first shell of the radial distribution function (the dotted purple circle). (b) Nearest-neighbor interaction versus radial separation.

We incorporate the filament nonlinearity to the extent that it effectively encodes the asymmetric response of the filaments to stretch and to compression; in this sense, our model is more "coarse-grained" than the well-studied "semi-flexible fiber" model[21]; the latter treats the bending degrees of freedom of F-actin based on the contour of the filaments using a continuum description. This bending effect, stated in our language of inter-bead interaction, essentially introduces a finite resistance/restoring force to compression in our originally buckling regime. It can be easily incorporated, yet we do not expect any qualitative modification on the mean-field level predictions made by our current model.

Similar buckling bonds were used to study the statistical mechanics of a "cat's cradle" built on a regular lattice by two of us several years ago[22]. Here we also include a HS repulsion to account for the excluded volume of the F-actin and ABP aggregates, and also assume the cytoskeleton adopts an aperiodic amorphous structure characteristic of the disorder of biological cytoskeletal networks. Thus in our model system, localization is

achieved not only at a high concentration of beads via hard-core repulsions (topological caging), but also will occur upon network expansion due to bond stretching. The interplay between the nonlinearity of interaction due to bucklable bonds and the network architecture renders the thermodynamic state diagram nontrivial in terms of diverse mechanical phases. These equilibrium phases include persistent uniform liquid-like states, regions with a coexistence of frozen and liquid phases, and the possibility of a martensitic-like phase transition that signals a spontaneous symmetry breaking.

The average length of F-actin in an *in vitro* network can be adjusted by controlling the concentration of capping proteins (for example the concentration of gelsolin); a higher molar ratio of capping protein to actin results in shorter F-actin on average. Increasing the crosslink concentration promotes the formation of F-actin and ABP aggregates[23], and in turn increases the bead density. The bead density determines the average spacing between the beads, or equivalently, the average end-to-end distance of F-actin (r). When $r < L_e$ the elasticity of the fiber is entropic in origin, whereas the intrinsic elastic modulus of the fiber dominates when $r > L_e$. The effective stiffness of the interbead F-actin ($\beta\gamma$) is also variable; it is enhanced when filaments are bundled together to form structures with larger diameters[24]. Thermal fluctuations play a smaller role as filaments become stiffer.

To get a feeling about how the relevant biophysical parameters work out in our model system, we can first estimate the bead density ρ from experimental actin concentration. The typical actin concentration used for *in vitro* networks is 23.8μM which, if we assume the actin monomers to be spheres of diameter 5nm, corresponds to a volume fraction of 0.9×10^{-3}. The ABPs take up negligibly small volume compared to that taken up by actin. We further take the bead size to be 1μm and the F-actin as slender rods of cross section 5nm $\times$ 5nm, then if each bead concentrates five F-actin of length 6μm, $\rho = 1.2$ is needed to reach the given volume fraction; if five F-actin of length 10μm per bead then $\rho = 0.9$ (taking the bead diameter d to be the length unit). Thus ρ is adjustable, ranging from 0.1 to 1.4, by varying actin concentration and/or crosslinking properties. Since the filament aggregates are not perfectly dense-packed within the bead, they only take up a portion of the assumed bead volume; the modeled hard-sphere repulsion between the beads may overestimate the excluded volume effect. Yet the qualitative phase behavior of this model system should not be altered. In a first approximation, the cytoskeleton determines the mechanical properties of a cell; since the elastic modulus of a cell is in the range of 10^3 Pa, the corresponding effective stiffness $\beta\gamma$ is then estimated to be between 1 and 10 as converted into our model parameters. (The characteristic bead size is $d = 1\mu$m.)

B. Mean field approximations and the self consistent phonon (SCP) method

Instead of treating the bending degrees of freedom of F-actin directly, we focus on the motion of individual beads, located on the vertices of the network, in order to find the nonlinear elasticity as the bead density is varied. In the mean-field spirit, we tag a given bead as the central particle, and study its stability/response to the local mechanical environment.

We build the model system on top of an amorphous structure. In contrast to a regular lattice that usually has a unique equilibrium configuration as well as a definite coordination number for a specific lattice structure, amorphous systems must be appropriately averaged over non-vibrational disorder in the lattice which we take as quenched. A further mean-field approximation will be made in the present analysis to avoid detailing the configurational complexity of a random network. We will summarize the underlying topology of the amorphous solid in an assumed isotropic pair distribution function $g(r)$ for the fiducial configurations of the system. Such a treatment has also been used for molecular structural glasses. We then define nearest neighbors as those beads that sit within the "first shell", i.e., up to the first minimum of the equilibrium radial distribution function $g(r)$, and assume that interaction only exists between nearest-neighbor pairs.
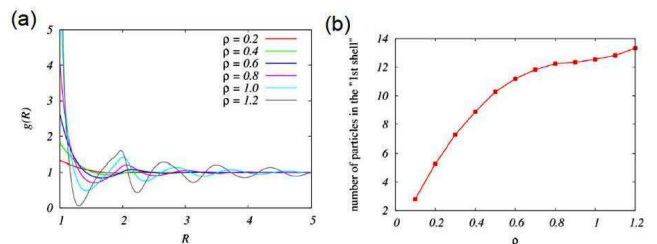

FIG. 2: (a) Radial distribution function $g(R)$ vs the radial separation R for a series of particle density ρ. As density increases, oscillatory amplitude gets larger along with a phase shift toward the core. (b) Coordination number vs particle density.

For liquids above the melting point, g_{HS} is well described by the Percus-Yevick approximation; the Verlet-Weis correction improves the behavior of $g(r)$ near the core and dampens its oscillations at large r, giving accurate modifications especially at high densities[25]. We follow the procedures of Verlet and Weis, and note that coordination number in an amorphous structure depends on particle concentration, because the amplitude and phase of the oscillations in radial distribution vary with number density/packing fraction of the particles (See Fig. 2(a)). As shown in Fig. 2(b), an increasing number of nearest neighbors are accommodated within the first shell when particles are packed denser. This increase is almost linear

when ρ is low, and slows down as ρ approaches 0.6; the modest increase above densities of 0.8 is bounded by the random close packing value of the coordination number which is around 14.

In the context of our model network, the amorphous topology effectively contains the physical aspects of bond breaking and/or ABP detachment upon network expansion. These aspects were absent in the lattice setting which was studied earlier: as the density of beads decreases (or equivalently as the network expands), coordination number drops off resulting in a smaller number of interacting neighbors or an effectively weaker network connectivity, even though the bond connections between each nearest-neighbor pair are assumed to be permanent at each given bead density.

As an approach of thermal stability analysis in an equilibrium system, the SCP theory was first developed to treat the anharmonic effects of hard-sphere crystals. The basic idea is to introduce a reference harmonic system, and then obtain the effective potential felt by each tagged particle, by averaging the pair interaction over the assumed Gaussian fluctuations from all its neighbors. This procedure should give back the assumed harmonic potential of the typical particle. The resulting coupled set of self-consistent equations allows an iterative scheme to determine the generally site-dependent force constants. Among several schemes, Fixman's SCP method based on a systematic expansion in Hermite functions has proven an efficient and especially robust procedure[26]. Recently, this technique has been applied to network glasses[27], and also by two of us to study motorized particle assembly[28] to analyze the far-from-equilibrium dynamics like that of the living protoplasm using a local feedback scheme.

We apply the SCP method to quantify the responses of various mechanical phases under varying physical conditions. At low concentration of beads, the effective attraction due to stretched springs dominates, thus the tagged particles are localized by "bond trapping"; whereas in the high concentration limit, HS repulsion dominates and results in a glassy/jammed state owing to "topological caging". To investigate both localized phases and the intermediate states that bridge the transition, we make a Gaussian local density profile ansatz with a single parameter, i.e. we describe the time-averaged density configuration as a sum of Gaussians representing thermal vibrations of particles about the fiducial sites

$$\rho(\vec{r}) = \sum_i \left(\frac{\alpha_i}{\pi}\right)^{3/2} e^{-\alpha_i(\vec{r}-\vec{R})^2}. \quad (2)$$

In the present work, the force constants (inverse mean squared displacements or localization strengths) $\{\alpha_i\}$ will all be taken to be equal, but it is not difficult to allow spatial variation[29], i.e., dependence on the index i.

In the independent-oscillator version of the SCP theory, the effective potential between two interacting particles is given by

$$e^{-\beta V^{eff}(|\vec{r}-\vec{R}'|;\alpha)} = \left(\frac{\alpha}{\pi}\right)^{3/2} \int d\vec{r}'\, e^{-\beta\frac{1}{2}V(\vec{r}-\vec{r}')}e^{-\alpha(\vec{r}'-\vec{R}')^2}, \quad (3)$$

which may be explicitly written as

$$
\begin{aligned}
e^{-\beta V^{eff}(R;\alpha)} &= \sqrt{\frac{\alpha}{\pi}}\frac{1}{R}\int_0^\infty dw\, w\, e^{-\frac{1}{2}\beta V(w)} \\
&\times \left[e^{-\alpha(w-R)^2} - e^{-\alpha(w+R)^2}\right]. \quad (4)
\end{aligned}
$$

Here, R denotes the averaged equilibrium separation between interacting particles, and α represents the homogeneous localization strength.

Taylor expansion of the effective interaction up to the second order gives a self-consistent relation for α:

$$\alpha = \frac{\rho}{6} \int_{\text{``1st shell''}} d^3\vec{R}\, g(\rho, R)\, Tr\left[\nabla\nabla\beta V^{eff}(R,\alpha)\right], \quad (5)$$

or

$$\alpha = \frac{2\pi}{3}\rho \int_1^{R^*} dR\, R^2 g(\rho, R)\nabla^2\beta V^{eff}(R,\alpha). \quad (6)$$

Here R^* marks the position of the first minimum of the radial distribution function $g(R)$. The HS diameter d, as the lower limit, is taken to be the unit of length.

C. Thermodynamic ramifications of our model system

We shall show in a moment that in our model system— a rigidly cross-linked nonlinear-elastic network—there exist at least two different localized phases: one modestly localized phase describes the weakly trapped motion due to bond stretching. We refer to this state as the "liquid-like state", in view of its considerable mobility and small localization strength (α_{liq}). The other more strongly localized state corresponds to the jammed motion within topological cages of neighbors. This solution depicts a "glassy state" exhibiting highly restricted vibrations (α_{gl}).

Traditionally, microscopic treatments of liquids take the view that since the liquid structure is dominated by repulsive forces, it is desirable to develop perturbation theories based on a HS reference system and then find the optimal parameters for it. In this spirit, the Helmholtz free energy can be obtained by adding a first-order perturbation to the free energy of the corresponding HS system. On the other hand, the Carnahan-Starling equation of state gives accurate values of the reference free energy at moderately high densities. In sum, the free energy for the liquid-like state is given by

$$
\begin{aligned}
f_{liq} &\equiv \frac{\beta A_{liq}}{N} = \left(\ln \rho\Lambda^3 - 1\right) + \int_0^\eta \left(Z_{CS}(\eta') - 1\right)\frac{d\eta'}{\eta'} \\
&+ \rho \int_{1st\,shell} d\vec{R}\, g(\eta, R) \\
&\times \left[\beta V_{model}^{eff}(R, \alpha_{liq}; \beta\gamma, L_e) - \beta V_{HS}^{eff}(R, \alpha_{liq})\right]. (7)
\end{aligned}
$$

Here the first term gives the entropic cost when all the nearest-neighbor pairs are bonded, with Λ denoting the thermal wavelength. The second term is the excess free energy of the HS reference system where the compressibility factor Z is given by Carnahan-Starling(CS) equation of state. The last term involves the energetic contributions from the attraction due to bond stretching; note the HS part is carefully deducted.

We use SCP theory to describe the free energy of glassy configurations[30,31]. The expression we use for an individual glassy configuration is

$$f_{gl} \equiv \frac{\beta A_{gl}}{N} = \rho \int_{1st\,shell} d\vec{R}\, g(\rho, R)\beta V_{model}^{eff}(R, \alpha_{gl}; \beta\gamma, L_e)$$
$$+ \left\{ \frac{3}{2}\ln\left(\frac{\alpha_{gl}\Lambda^2}{\pi}\right) - 3\ln\left[erf(\sqrt{\alpha_{gl}}D)\right] \right\} - \delta f. \quad (8)$$

Here the first integral gives the "on-site" free energy after double averaging over thermal fluctuations and over topological disorder. The second term (inside the curly bracket) comes from $-(1/N)\ln\left[Z_p \cdot \left(\int_{|w_i|\leq D} d\vec{w}\,e^{-\alpha w^2}\right)^N\right]$ which accounts for the effect of cell constraint; Z_p represents the momentum part of the partition function, and we choose a cubic cell with side length $D \equiv \rho^{-1/3}/2$ for convenience. Finally, δf (taken to be 0.224) is a numerical correction to the entropy of HS crystal system near face-centered-cubic (fcc) close packing obtained via SCP approximation, which then gives extremely accurate free energies near melting.

The pressure can be evaluated by numerically differentiating the liquid free energy:

$$p = \rho^2 \left(\frac{\partial}{\partial \rho} f_{liq}\right)_{T,N} k_B T. \quad (9)$$

Random first order transition theory identifies the configurational entropy with the difference between the free energy of the highly localized glass solution and the liquid, i.e.

$$\frac{S_c(\rho, \beta)}{Nk_B} = \Delta f = f_{gl} - f_{liq} \quad (10)$$

Another interesting quantity that can be evaluated within the SCP theory is the number of force-bearing bonds, i.e., those that have a length exceeding the elasticity onset L_e. In three dimensions, the structure-dependent probability for a single bond to be elastically stretched (or equivalently, the fraction of stretched bonds, in the mean field context) is given by

$$q_3(\alpha, R) = \int_{|\vec{r}|>L_e} d\vec{r} \left(\frac{\alpha}{\pi}\right)^{3/2} e^{-\alpha(\vec{r}-\vec{R})^2}, \quad (11)$$

or

$$q_3(\alpha, R) = \sqrt{\frac{\alpha}{\pi}} \frac{1}{R} \int_{L_e}^{\infty} dr\, r \left[e^{-\alpha(r-R)^2} - e^{-\alpha(r+R)^2}\right]. \quad (12)$$

The number of stretched bonds can then be obtained by averaging over non-vibrational disorders, i.e. configurational degrees of freedom:

$$q_3(\alpha, \rho) = \rho \int_{1st\,shell} d\vec{R}\, g(\rho, R)q_3(\alpha, R). \quad (13)$$

This double integral accounts both for the contributions from the fluctuation of individual bonds (small α indicates strong fluctuation) and from fluctuations in the underlying topological structure (short L_e enlarges the radial range that contains stretched "fiducial bonds").

III. NUMERICAL INVESTIGATIONS

A. Localization strength

The fundamental quantity that characterizes the diverse mechanical phases in our model is the localization strength, or the force constant of the emergent Einstein oscillator, α. We may plot α against bead density ρ and/or effective stiffness $\beta\gamma$ of the F-actin. We measure lengths and energies in units of d and β, then the corresponding dimensionless quantities are taken to be $\rho^* \equiv \rho d^3 = \rho$ and $\gamma^* \equiv \beta\gamma d^2 = \beta\gamma$. We start with several representative one dimensional plots that come from vertical slices of the two dimensional α-surface, and we first focus on the liquid-like solution which is absent in the pure HS system.
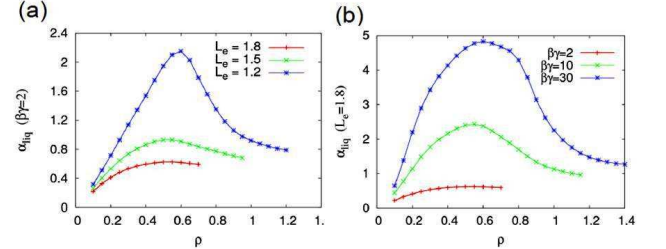
FIG. 3: Liquidlike localization strength α_{liq} versus bead density ρ. (a) For $\gamma^* = 2$ with $L_e = 1.2$ (blue), 1.5 (green), 1.8 (red); (b) for $L_e = 1.8$ with $\gamma^* = 2$ (red), 10 (green), 30 (blue).

Referring to Fig. 2(a), we observe that the first shell (R^*) of the radial distribution shrinks from 1.95 to 1.3 as the bead density increases from 0.2 to 1.2. When $L_e < R^*$, the separation ($R^* - L_e$) determines how many nearest-neighbor fiducial sites are found beyond L_e and on-average have tense bonds; in this case, both the underlying topology and thermal fluctuations contribute to the localization. On the other hand, however, if $L_e > R^*$, all fiducial sites of nearest neighbors fall inside the sphere of radius L_e and on-average result in buckled strings; in this case fluctuations are the only source of stretching and thus of localization. This information is also encoded in

the *threshold density* ρ_{th} beyond which a stable α_{liq} solution no longer exists. In sum, longer onset length leads to weaker overall localization as well as lower threshold density, as shown in Fig. 3(a). A similar effect is produced by low rigidity γ as can be seen in Fig. 3(b); since smaller γ indicates a broader and shallower confining well in which particles are more loosely tethered thus being less localized, and the corresponding liquid-like solution becomes unstable at lower ρ_{th}.
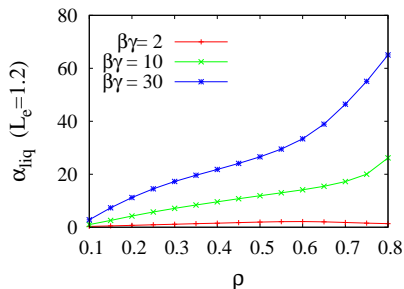

FIG. 4: Liquidlike localization strength versus bead density for $L_e = 1.2$ with $\beta\gamma = 2, 10, 30$. Liquid-like solution is still distinct at $\beta\gamma = 2$, whereas a rapid crossover to glassy behavior occurs for $\beta\gamma = 10, 30$.

The compromise between the number of contributing neighbors and the degree of stretching produces a non-monotonic density dependence of α_{liq} at a given L_e, and the most efficient localization is achieved at an intermediate density around 0.6. At $\rho < 0.6$, the individual bonds become less likely to be stretched as the beads pack more densely, whereas the total number of bonded neighbors increases much faster with increasing density, the combined effect thus leads to a stronger localization as density grows. On the other side when $\rho \geq 0.6$, the number of bonded neighbors almost saturates, while the thinner first shell of g(r) indicates less tightly stretching or deeper buckling as density increases, whereby the localization strength decays accordingly.

Note that this non-monotonic density dependence only occurs for a sufficiently long L_e or in the low-$\beta\gamma$ regime for a short L_e. For sufficiently high $\beta\gamma$ liquid-like solutions are no longer distinct, instead a rapid crossover to high-α solutions is observed, as is exhibited in Fig. 4.

B. Thermodynamics

1. q_3—role of localization

Recall that q_3 explicitly counts the average number of tensely bonded neighbors. Its dependence on elasticity comes from the self-consistently determined localization strength α and the intrinsic cutoff L_e for a bond to be stretched. For a given ρ, more elastically-bonded neighbors become available as L_e drops (Fig. 5(a), bottom to top) and/or γ^* decreases (Fig. 5(b), bottom to top). For a moderate γ^*, the number of stretched bonds increases

with bead density for various L_e as long as stable liquid-like solution exists (Fig. 5(a)); at high γ^*, however, close to the most localized regime for individual beads, even though the coordination number still gently increases, the weak fluctuation (high α) strongly suppresses bond stretching, thus leading to an intermediate decline of q_3 in its ρ-dependence, as seen in $\gamma^* = 10, 30$ cases (Fig. 5(b)).
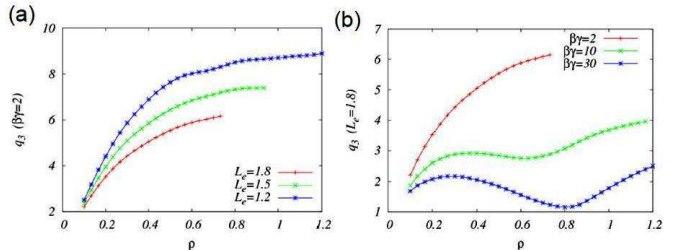
FIG. 5: Average number of stretched bonds q_3 vs bead density ρ. (a) $\gamma^* = 2$ for $L_e = 1.2, 1.5, 1.8$ (top to bottom); (b) $L_e = 1.8$ for $\gamma^* = 2, 10, 30$ (top to bottom).

2. free energy profile—consistency with SCP theory
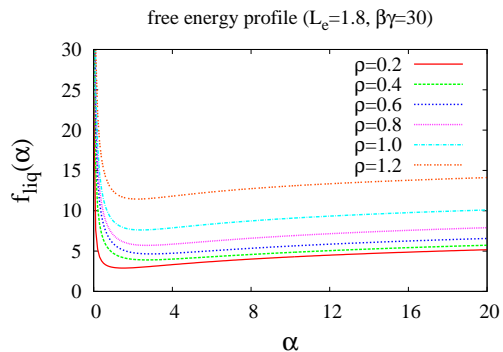
FIG. 6: Free energy f_{liq} versus the order parameter—localization strength α with $L_e = 1.8, \beta\gamma = 30$ for $\rho = 0.2$–1.2 (bottom to top). As the bead density ρ increases, the overall profile shifts upward with the valley indicating the equilibrium solution α_{liq}.

As can be seen when we compare Fig. 6 with the corresponding curves in Fig. 3(b), the minima on the free energy profile $F(\alpha)$ for the liquid-like state coincide with the corresponding α_{liq} solutions obtained via the SCP method. As the bead density increases, the overall profile shifts upward. At a given density ($\rho = 0.6$ here), raising L_e (Fig. 7(a)) or lowering γ^* (Fig. 7(b)) causes the liquid-like state to be increasingly favorable (deeper and sharper valley) with lower localization strength (bottom of valley being shifted leftward). As expected, γ^* only markedly affects the low-α regime ($\alpha \leq 10$), since when particles are sufficiently localized (due to short L_e or high ρ), bond stiffness only plays a minor role in altering the

FIG. 7: Free energy versus localization strength. (a) $\gamma^* = 2$ for $L_e = 1.2, 1.5, 1.8$ (top to bottom); (b) $L_e = 1.8$ for $\gamma^* = 2, 10, 30$ (bottom to top).
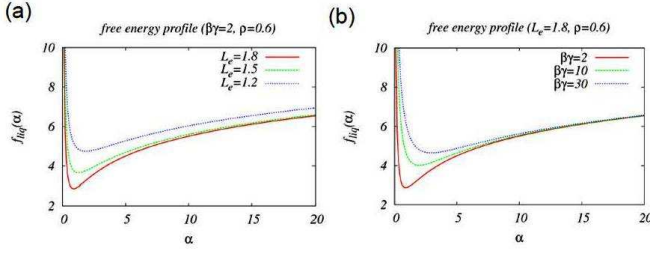

FIG. 8: Pressure versus bead concentration for soft strings ($\beta\gamma = 2$) with various onset lengths $L_e = 1.2, 1.3, 1.4, 1.5$ (bottom to top). Main plot: total pressure; inset: pressure due to attraction.

interaction strength. In contrast, varying L_e not only modulates the low-α regime, but causes a nearly uniform upshift of the high-α portion of $F(\alpha)$; this observation is consistent with our previous statement that when thermal fluctuations are weak (high α) topology dominates; shorter elasticity onset L_e indicates more stretched bonds at a given density and thus enhanced interaction.

3. pressure

We plot pressure versus bead density with $\gamma^* = 2$ for a series of onset lengths in Fig. 8. At the low-density end, most of the bonds are stretched and the system tends to shrink, resulting in a very low pressure. At the opposite end, in a densely packed system HS repulsion takes over the major role; the steeply increasing pressure reflects the rising difficulty in rearrangement and the consequent soaring resistance to compression. In contrast with the nearly universal behavior at both extremal-ends, parameter-sensitive features emerge in the intermediate density regime, where shorter L_e enhances the effective attraction and thus lowers the pressure of the system. In particular, a non-monotonic behavior is observed to occur for pliable springs (low γ^*) with early onset (short L_e), as is exhibited for the case of $L_e = 1.2$.

It is natural to expect the possibility of a negative pressure at a modest bead concentration in view of the tendency of the network to shrink due to attraction. We plot in the inset of Fig. 8 the contribution of attraction (p_{attr}) to the total pressure (p_{tot}) for several onset lengths, and p_{attr} does indeed exhibit a negative valley at intermediate concentrations. It is clearly seen that a short onset length is necessary for a notable contribution from attraction and thus for the emergence of this non-monotonic behavior of the total pressure.

On the other hand, the negative contribution owing to attraction is eventually overwhelmed by the positive part due to a more rapid increase in repulsion as ρ increases, and the total pressure (p_{tot}) remains positive over the whole density range. This behavior is originated from the specific form of the free energy functional that we have used for the model system, where the correction due
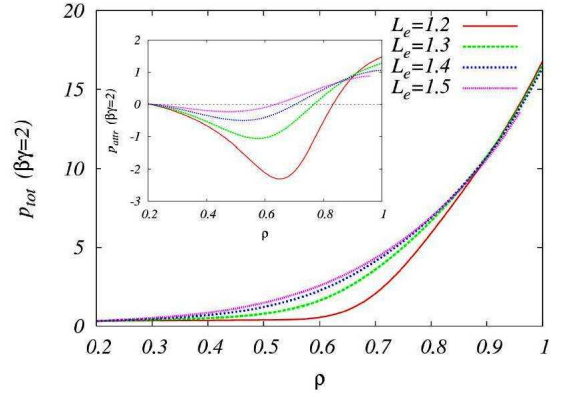
to attraction enters as a perturbation to the dominating repulsive part. This result might require modification to better accommodate the low-concentration regime where attraction becomes important. Another reason for this behavior may be related to the $g(r)$ we have used for the radial distribution which drops sharply when move away from the core; bonding effects might lead to a fatter tail of $g(r)$ and an enhanced contribution from attraction. Nevertheless, we feel these insufficiencies of the approximations should not modify the mechanical and thermodynamic properties qualitatively.

The thermodynamic considerations discussed above help with understanding of the physics underlying the predicted phase behavior in terms of the order parameter α. We will discuss these in detail next.

C. State diagram

1. Overview

In our model network, we assume permanent bond connections between the nearest-neighbor pairs. The interplay between these intrinsic constraints and the thermal fluctuations gives rise to an inhomogeneous distribution of tensile forces throughout the network. Such force heterogeneity exhibits as a (uniform) non-vanishing tethering strength in our mean field context. This explains the prediction that a completely ergodic fluid phase, which is allowed for the pure hard-sphere system with short-range attraction and that has strictly diffusive behavior for long times i.e. $\alpha \to 0$ as $t \to \infty$, never occurs for the equilibrium network structure; the lack of utter freedom in locomotion leads to a *finite* α over the whole span of bead concentrations.

There exist two characteristic densities in our model system: the threshold density ρ_{th} above which the ho-

mogeneous liquid-like solution is no longer stable, and the critical density ρ_{cr} which signals the emergence of a glassy state. These densities help define the boundaries between diverse mechanical phases:

- $\rho < \rho_{th}, \rho_{cr}$: only α_{liq} exists, which describes the liquid-like loosely tethered phase;
- $\rho_{th} < \rho < \rho_{cr}$: the mean-field α_{liq} is no longer stable, and the glassy state has not yet occurred; bifurcation to a low-α solution may occur, exhibiting a symmetry broken phase which we shall call the "martensitic-like" (ML) phase;
- $\rho_{cr} < \rho < \rho_{th}$: both α_{liq} and α_{gl} exist, depicting the transition state with presumably coexisting phases that implies a macroscopic number of configurational degrees of freedom for structural rearrangements.
- $\rho > \rho_{th}, \rho_{cr}$: the repulsive-glass phase dominates.

2. Features of the various phases

Our SCP calculation has found five distinct phases in our model system: the liquid-like (LL) phase, the crossover (CO) phase, the repulsive-glass (RG) phase, the multiple-solution (MS) phase, and a martensitic-like (ML) phase.

◇ the liquid-like (LL) phase and crossover (CO) phase

We choose two particular onset lengths based on their position with respect to the boundary of the nearest-neighbor shell.

For $L_e = 1.8$, this cutoff stands outside the nearest-neighbor shell for $\rho : 0.2$–1.2, which means that almost all the "fiducial bonds", i.e. bonds that connect fiducial sites of nearest neighbors, are buckled, and become more floppy as bead density grows; in this situation once the coordination number saturates at $\rho \simeq 0.6$, increasingly deeper buckling results in a decrease in α_{liq} as ρ increases. Owing to the overall buckling of the bonds, higher bond stiffness and thus smaller fluctuations lead to a smaller probability for the bonds to tense up, and an even steeper drop in α_{liq} occurs as density increases (Fig. 3(b)). Therefore, the distinct liquid-like solutions persist over the whole γ^*-range of interest (as long as $\rho \leq \rho_{th}$) for the case of a long onset length.

For the case of $L_e = 1.2$, however, since this cutoff remains inside the nearest-neighbor shell all the way through $\rho : 0.2$–1.2, there always exists a fraction of fiducial bonds being stretched beyond their relaxed length. In this situation the descending branch of α_{liq} at intermediate densities only occurs for very soft springs, i.e. in the low-γ^* regime. Furthermore, taking advantage of the persistent fraction of stretched (fiducial) bonds, sufficient stiffness beyond a threshold value (marked by the phase boundary ρ_{CO}) would help enhance localization, and facilitates a smooth crossover from elasticity-dependent liquid-like behavior to geometry-dominant glassy behavior (as seen in Fig. 4); we shall refer to the states showing such behavior as being in a "crossover" (CO) phase.

◇ the repulsive-glass (RG) phase

Current simulations performed on increasingly longer timescales make it possible to compare the equilibrium properties based on the present theoretical predictions with simulation outcomes in the long-time limit. To investigate the long-term fate of attractive glasses, simulations of glassy arrest in hard-core particles with short-range attraction[32] were performed over a waiting-time-independent window of up to 10^6 MD units, which is a few orders of magnitude longer than those reached by previous experiments or simulations ($\sim 10^3$ MD units). They found that even if the short-range attraction generates a transient plateau in the time-evolution of the calculated mean-squared displacement (i.e. inverse α) owing to breaking and reforming of nearest-neighbor "bonds", the long-time behavior of "bonded" and "nonbonded" repulsive glasses converges, suggesting that in the long run particles are ultimately confined by their topological cage of neighbors.

Our equilibrium calculation on a long-range-attractive HS system consistently shows that as long as the (nearly-universal) critical density is reached, there would emerge the repulsive-glass behavior being almost independent of the attractive strength γ^*. Such independence is found for various onset lengths.

◇ the multiple-solution (MS) phase

The simultaneous presence of distinct α_{liq} and α_{gl} solutions, according to the SCP analysis, implies a non-vanishing configurational entropy in this phase region. This further signifies the availability of configurational degrees of freedom for structural rearrangement. As shown in previous examples, a longer onset length ($L_e = 1.8$) allows for distinct α_{liq} solutions over a larger $\beta\gamma$ range and thus allows the system to explore more energetically favorable configurations; on the other hand, the emergence of crossover behavior at moderate $\beta\gamma$ and the consequent shrinkage of the MS regime induced by early onset of elasticity ($L_e = 1.2$) suggests a rapid loss of configurational entropy as bonds become stiffer.

◇ the martensitic-like (ML) phase

As verified by our SCP calculation, a completely ergodic fluid phase, presented by a sticky HS system with weak attraction at a low density, does not occur for an elastically bonded HS system, so that α is always finite. Yet finite localization strength does not ensure a homogeneous structure. In our model system, with a large elasticity onset L_e (compared to the lattice spacing) and a low bond stiffness γ^*, bifurcation in α_{liq} takes place before the emergence of glassy behavior (i.e. below ρ_{cr}) and may allow the existence of a spatial-symmetry-broken phase characterized by a stable pair of liquid-like solutions. The occurrence of bifurcation was also found in an earlier study by Shen and Wolynes with a pure "cat's cradle" built on a regular lattice. The possibility of self-generated spatial heterogeneity associated with such a mechanical instability makes it interesting to study what kind of structural phase such a destabilized system would actually develop into, and to quantify the associated conformational changes. The resultant me-

chanical/structural phase might be related to the orientational order often observed in F-actin networks of the cytoskeleton.

We performed explicit molecular dynamics (MD) simulations on a body-centered-cubic (BCC) network of n^3 unit cells with pure nonlinear elasticity, as described by the Hamiltonian $H = \frac{1}{2}\sum_i \sum_{<j>} \frac{1}{2}\gamma \left(|\vec{r_i} - \vec{r_j}| - L_e\right)^2 \Theta\left(|\vec{r_i} - \vec{r_j}| - L_e\right)$.
Here i,j label the nodes and $\langle \cdots \rangle$ represents sum over nearest neighbors; γ denotes bond stiffness and L_e elasticity onset as before. The bipartite nature of the BCC structure allows us to divide the original BCC network into two interpenetrating simple-cubic (SC) subnetworks (see an illustration of the subnetwork division in Fig. 9(a)) , so that each node on one subnetwork interacts with its 8 neighbors on the other subnetwork, and the neighbor list never changes.

The quality of the motion—whether it is oscillatory or monotonic—depends on the relative contribution of the inertial forces (that tend to produce oscillations) and the viscous forces (that tend to damp the oscillations out). It turns out that inertial forces are usually very small at the microscopic and molecular levels, so that the overdamped limit usually applies[1]. We thus carried out the simulations with stochastic dynamics in the overdamped limit as described by the Langevin equation $d\vec{r_i}/dt = (1/\Gamma)\vec{f_i}(t) + \vec{\eta_i}(t)$. Here $\vec{f}$ represents the deterministic force due to the nonlinear elastic interaction, and the force exerted by the fluid particles divides into two parts: the average viscous force $-\Gamma\vec{v}$ and a random force $\vec{\zeta}(t) \equiv \Gamma\vec{\eta}(t)$ whose time average is zero. We assume a Gaussian white noise that satisfies $\langle \eta_i(t)\eta_j(t')\rangle = 2D\delta_{ij}\delta(t - t')$. As usual, Γ and D denote the drag coefficient and diffusion constant, respectively. Lengths are expressed in units of L_e. We applied periodic boundary conditions.

We first show the evolution of the mean squared displacement (MSD) with respect to the *initial* equilibrium positions of the nodes. We simulated a system of size 5^3 with soft bonds ($b \equiv \beta\gamma = 1$) at a low temperature ($\beta = 30$). When the elasticity onset L_e is comparable with the initial mesh size, R, of both subnetworks, elastic stretching is immediately felt as soon as thermal buffeting displaces any of the nodes from their equilibrium locations, and therefore, the whole network just wiggles about the underlying BCC lattice, which defines the unique minimum of the system's energy landscape. As shown in Fig. 9(b), in this case the two subnetworks act in a concerted manner with their mean squared displacements fluctuating almost "in phase", suggesting the whole BCC network does not show symmetry breaking.

When the system parameters are modified to be in the regime of bifurcation by increasing the L_e/R ratio to 10 (other parameters unchanged), however, the MSD exhibits a much larger average amplitude (after a steady value is reached) and stronger fluctuations around it; furthermore, the two subnetworks fluctuate in a correlated manner but are almost completely out of phase with each
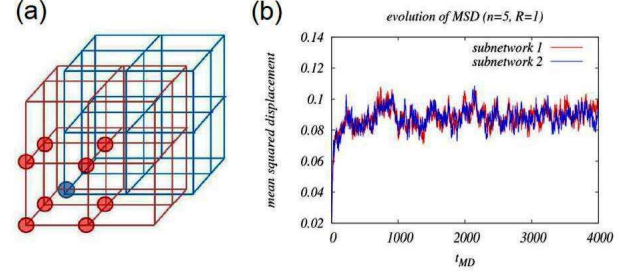
FIG. 9: (a) An illustration of the subnetwork division. The bipartite nature of the original BCC lattice allows for separation of one SC subnetwork (red) from the other (blue). Each node on one subnetwork (blue sphere) interacts with its 8 neighboring nodes (red spheres) on the other subnetwork. (b) The MSD of both subnetworks ($n = 5$) versus simulation time in MD units for a moderate elasticity onset to mean separation ratio $L_e/R = 1$. $\Gamma = 50, \beta = 30$.
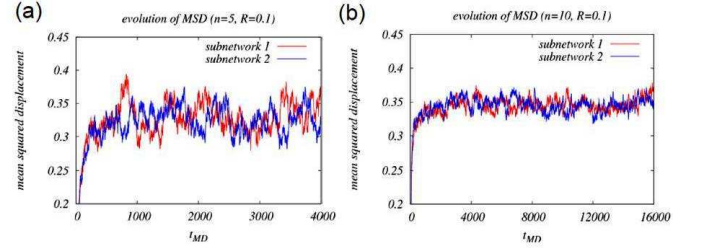
FIG. 10: Effect of the system size on the behavior of MSD in the regime of bifurcation. Both: $L_e/R = 10, \Gamma = 50, \beta = 30$. (a) $n = 5$; (b) $n = 10$.

other, see Fig. 10(a). In this case, the initial network presents no elastic constraints on the nodes, thus the system is free to expand until it reaches a steady size where the mean separation between the bonded neighbors is comparable with the length for elasticity onset; the correlated fluctuations result from alternate distortions between the subnetworks within a system of moderate size as 5^3. As we enlarge the system to $n = 10$ (Fig. 10(b)), the steady amplitude of MSD maintains ($\sqrt{MSD} \sim 0.6$ stretching could occur under thermal driving), yet the fluctuations about the average become much weaker.

The above observation raises the intriguing possibility of a "martensitic-like" phase consisting of (frustrated) domains with (complementary) distortions. To examine further this possibility, we also queried vectorial information about the directions of motion (lost in MSD) by examining the evolution of displacement vectors. We divided the simulation cell evenly along each initial dimension to get 8 domains each with the same number of nodes, and traced the subsequent motion within each domain. We chose a time window $t_{MD} = 4000$–6000 after the steady size was reached, and used the running time averaged position of the nodes as the reference with respect to which the displacements were defined.

We present in Fig. 11 the bulk-averaged (left column) and domain-averaged (right column) displacement components. The evolution of the displacement vectors in these two cases shows several contrasting features. First, the maximal amplitude of the domain-averaged displacements is about one order of magnitude larger than the maximal amplitude of the bulk-averaged displacements. Second, the bulk-averaged displacements of the two subnetworks are exactly oriented in the opposition directions with essentially the same amplitude, whereas in individual domains two subnetworks move almost in the same direction yet with different amplitudes. These two contrasting features support the picture of localized distortions with different orientations in different domains. In addition, the peak value of the displacement amplitude occurs at different times for different domains, which suggests "frustration" between the domains.

FIG. 11: The bulk-averaged and domain-averaged displacement components for both subnetworks. $n = 10, L_e/R = 10, \Gamma = 50, \beta = 30$. (a)-(c) average over the whole simulated region; (d)-(f) average over one of the 8 domains. (a)(d) x component; (b)(e) y component; (c)(f) z component.

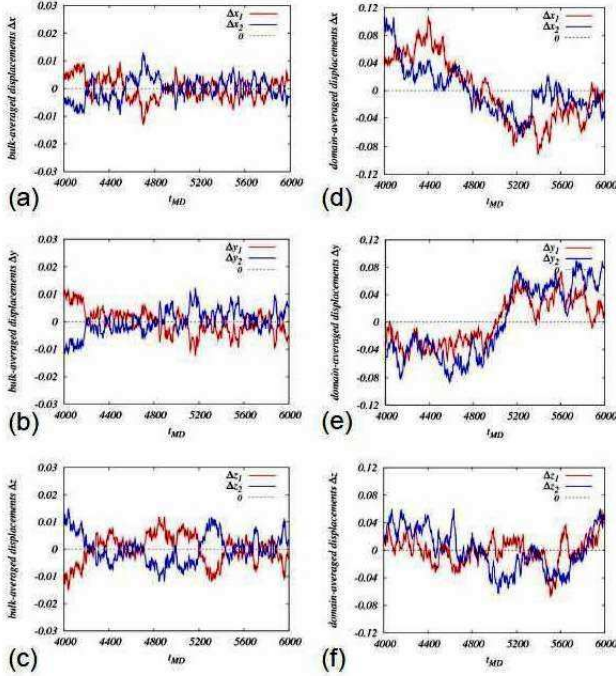To roughly estimate the domain size and to quantify the orientational correlation within the domains, we made equal-width shells centered at each node (the diameter of the outermost shell was taken to be equal to the box size of the simulated system), and computed two measures: (1) the average projection of director (i.e. the unit vector of the corresponding displacement) in each shell onto that of the central node, and then averaged over all possible central nodes. In mathematical terms, we monitor $P_m(t) \equiv (1/N) \sum_{i=1}^{N} \hat{r}_i(t) \cdot$

$\left(\frac{1}{N_m} \sum_{j_m=1}^{N_m} \hat{r}_{j_m}(t) \right)$, where N is the total number of nodes and N_m the number of nodes within the mth shell of the central node; $\hat{r}_i$ and $\hat{r}_{j_m}$ are instantaneous directors of the central and in-shell nodes, respectively; (2) the average tensor product of directors constructed as $Q_m(t) \equiv (1/N) \sum_{i=1}^{N} (\hat{r}_i(t) \cdot \hat{y}) \left(\frac{1}{N_m} \sum_{j_m=1}^{N_m} (\hat{y} \cdot \hat{r}_{j_m}(t)) \right)$, where $\hat{y}$ is the unit vector pointing from the instantaneous position of node i to that of node j_m. This measure thus reflects the degree of alignment of two directors along the line connecting their positions.
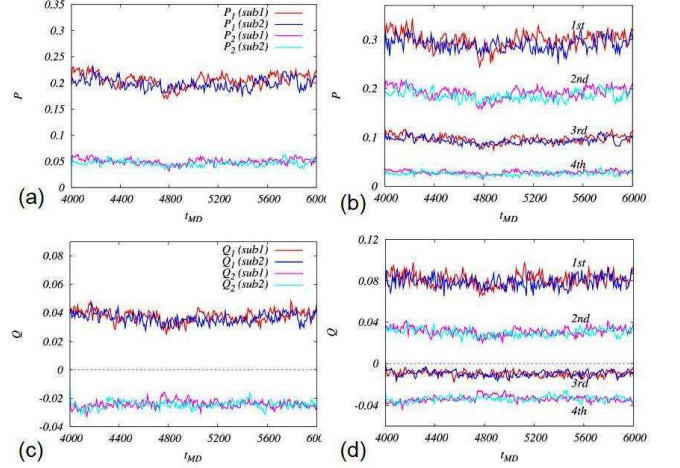
FIG. 12: The evolution of two measures of the orientational correlation for both subnetworks. $n = 10, L_e/R = 10, \Gamma = 50, \beta = 30$. (upper) the average director projection P for 2 shells (a) and 4 shells (b); (lower) the average tensor product of directors Q for 2 shells (c) and 4 shells (d). In each panel, shown from top to bottom are values of the measure from the inner to the outer shell(s); red/magenta denotes subnetwork 1, and blue/cyan denotes subnetwork 2.

We show in Fig. 12 the evolution of these two measures for the cases of 2 shells (left column) and 4 shells (right column). The average director projection P, in each shell, fluctuates about a steady value, which decays from around 0.2 to 0.05 as we go from the inner to the outer shell in the case of 2 shells (panel (a)). This spatial decay in average P indicates that the domain size is roughly half of the box size, i.e., 5 times the initial lattice spacing. As expected, the fluctuations in P become weaker for outer shells due to the larger number of nodes to be averaged over; this trend is clearly exhibited in the case of 4 shells (panel (b)).

In contrast to the positive steady value of P in all shells, the average tensor product of directors Q becomes negative for the outer shell(s) (lower panels of Fig. 12). Since Q encodes the angular location of the in-shell node relative to the central node, a negative value of Q implies the two directors point in the opposite directions along the line that connects them. A stronger opposite alignment would give a more negative Q value. Q thus serves as an indicator of the loss in orientational correlation.

Also, negative Qs are smaller in amplitude than positive Qs.

To make the situation more apparent, we visualized the ensemble-averaged displacement vectors at different angles and different distances from the central node for the case of 2 shells (Fig. 13). We took the ensemble-averaged direction of motion of the central node as reference. Within the first shell (colored in pink) the average displacement in any angular range gives a positive projection on the reference direction, in other words, the displacement field is anisotropic and the movements occur mainly along the same direction as that of the central node. The aligned movement is most significant near the "equator". The displacement vectors in the second shell (colored in blue), however, no longer exhibit a preferred orientation, instead they reorient considerably. Close to the "south pole", the outward movements are almost perpendicular to the reference direction, whereas small inward movements occur near the "north pole". The spatial decay in orientational correlation is thus apparently observable and consistent with the features exhibited by our correlation measures.

FIG. 13: Average displacement vectors (purple arrows) at different angles and different distances (inner and outer shells) from the central node (red sphere). Shown for one cross section of the spherical region.

3. Typical examples

We plot the 2D surfaces of α_{liq} and α_{gl} against $\rho^*(=\rho)$ and $\gamma^*(=\beta\gamma)$ at a given L_e to examine how these physical parameters modulate the phase boundaries. The contour maps are a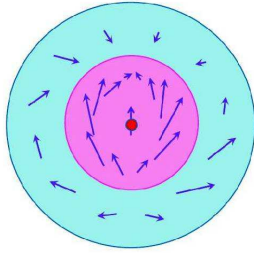lso projected on the bottom as reference for the upcoming state diagrams. We choose two particular values of the elasticity onset L_e that characterize typical tense networks ($L_e = 1.2$) and floppy networks ($L_e = 1.8$).
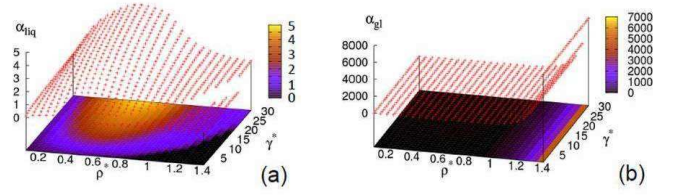
FIG. 14: 2D surface of localization strength over the parameter space extended by bead density (ρ^*) and elastic stiffness (γ^*) in the case of $L_e = 1.8$ characterized by mostly floppy bonds. Here ρ^* runs through 0.1 to 1.4 and γ^* ranges from 1 to 30. We show the α surface and its contour map for liquid-like (a) and glassy (b) solutions. The color scheme indicates the relative measure of the α values; the highest value within a given range is colored as bright yellow and the lowest as black.

We start with $L_e = 1.8$ case. For this relatively long onset length, liquid-like and glassy solutions are quite distinct over the whole parameter space. As can be seen from Fig. 14(a), the liquid-like localization strength takes on a "hump" shape along the ρ-axis peaking around $\rho = 0.6$, and elevates smoothly in the γ^* direction. However, the stable α_{liq} solution terminates at a sharp boundary defined by $\rho_{th}(\gamma^*, L_e)$ beyond which the mean field α_{liq} solution becomes destabilized. This instability region, located in the high-ρ low-γ^* corner, presents a quasi-triangular shape which indicates the increased need of stiffer bonds to stabilize the loosely arrested state as density increases. The ML phase may arise as a possible consequence of this (elastic-)nonlinearity-induced mechanical instability. On the other hand, α_{gl} emerges at $\rho_{cr} \simeq 1$. The values of the critical density and of α_{gl} are nearly independent of γ^*, as shown in Fig. 14(b); such stiffness-independence arises from takeover of the dominant role by HS repulsion in reconfiguring a densely packed system.

The corresponding state diagram on ρ-γ^* plane is displayed in Fig. 15(a). The trajectories marked by ρ_{th} (blue curve) and ρ_{cr} (dashed line) unambiguously divide the state space into four distinct phase regions: distinct liquid-like ($\rho < \rho_{th}, \rho_{cr}$) and glassy ($\rho > \rho_{th}, \rho_{cr}$) phases locate at the opposite corners diagonally, while the rest of the space naturally divides into the ML and the MS phases depending on whether $\gamma^* < \gamma_c^*$ ($\rho_{th} < \rho_{cr}$) or $\gamma^* > \gamma_c^*$ ($\rho_{th} > \rho_{cr}$), respectively. For a given L_e, ρ_{th} increases with γ^* whereas ρ_{cr} is topologically determined, consequently when $\gamma^* < \gamma_c^*$ and $\rho_{th} < \rho < \rho_{cr}$, the region of the ML phase narrows down as γ^* increases due to decreasing ($\rho_{cr} - \rho_{th}$) until it disappears at $\gamma^* = \gamma_c^*$ ($\rho_{th} = \rho_{cr}$); when $\gamma^* > \gamma_c^*$ and $\rho_{cr} < \rho < \rho_{th}$, the MS phase takes over and broadens as γ^* rises because of growing ($\rho_{th} - \rho_{cr}$).

In addition to the four types of phases exhibited by the floppy network ($L_e = 1.8$), the state diagram for the tense network ($L_e = 1.2$) presents a novel phase boundary separating out a large region featuring a crossover

In sum, in addition to the multiple solution regime which may be related to the saddle point solution pictured as ergodic droplets formed against a glassy background in a finite-range system, our mean-field level calculation also predicts a parameter regime where nonlinear-elasticity-induced spatial inhomogeneity is exhibited through a "martensitic-like" phase with local oriented distortions.

FIG. 15: The state diagrams of a typical floppy network with $L_e = 1.8$ (a) and a typical tense network with $L_e = 1.2$ (b). These diagrams are constructed against the corresponding contour maps of liquid-like and glassy solutions, summarizing all possible phases partitioned by transition boundaries. In the $L_e = 1.8$ diagram, γ_c^* marks the crossing point of ρ_{th} curve (blue) and ρ_{cr} (or ρ_A) line (black dashed). The "mechanical" diagrams are further integrated with thermodynamic characteristics — laboratory glass transition density ρ_G (green dotted line) and Kauzmann density ρ_K (red full line). The floppy network exhibits higher ρ_G and ρ_K than the tense network does.
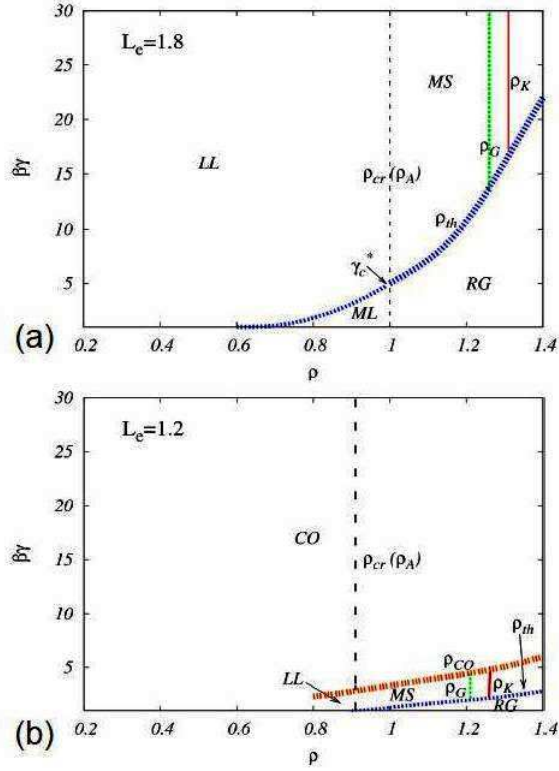
ness increase). Moreover, the ML phase doesn't emerge for tense networks since the instability is avoided by early elasticity onset.

Beyond the upper boundary of this stripe-shaped phase region, the α-surface gently mounts up toward the high-γ^* high-ρ^* direction and smoothly crossovers from the elasticity sensitive behavior to the glass-like behavior as ρ_{cr} is approached; consequently, in this crossover regime ρ_{cr} no longer marks a clear transition boundary. The resultant state diagram is presented in Fig. 15(b).
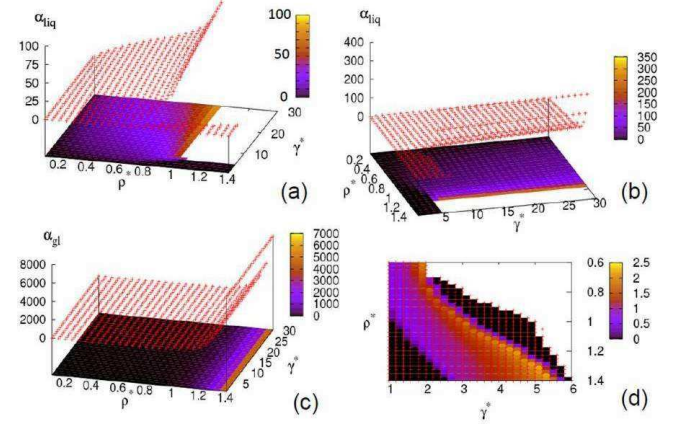
FIG. 16: 2D surface and contour map of the localization strength for the case of $L_e = 1.2$ that features a persistent fraction of tense bonds. Upper panels: liquid-like solutions up to $\alpha_{liq} = 100$ (a) and $\alpha_{liq} = 350$ (b). Both the peeling-off stripe-shaped region for distinct liquid-like solutions and the smooth crossover to glassy behavior are explicitly displayed. (d) Amplified contour map for the stripe-shaped region; (c) glassy solutions over the whole parameter regime.

4. Characteristic densities

Due to the bonding constraints inherent in a network structure, the stabilized state in our model always possesses a finite localization strength, i.e. $\alpha > 0$. Thus in this case the dynamical transition density ρ_{cr} (or called ρ_A as in literature), rather than being the lowest density to give a non-zero α as occurred in pure or sticky HS systems, is defined as the lowest density to trigger persistent high-α solutions over the whole γ^* range of interest. In our model system, ρ_{cr} signals the emergence of an extensive number of glassy metastable states, yet does not mark the termination of bonding effect.

While the SCP theory alone allows us to find ρ_A, the "Kauzmann density", ρ_K, at which the Helmholtz free energies of the liquid-like and glassy phases match and the configurational entropy ceases to be extensive also relies on the specific form of the free energy functionals we use for these two types of states. The ratio ρ_A/ρ_K dimensionlessly characterizes the thermodynamic aspects. To connect to the kinetic laboratory glass transition, we note

behavior. When we compare the 2D surface for α_{liq} with that for α_{gl} over the whole parameter plane, we find that they almost coincide except for a stripe-shaped region in the low-γ^* high-ρ^* corner. When we zoom in on this region (contour map shown in Fig. 16(d)) that peels off the smoothly ascending α-surface (see upper panels of Fig. 16), we observe that the diagram appears like a "squeezed version" of that for the $L_e = 1.8$ case; namely, α_{liq} also exhibits a non-monotonic density dependence, and ρ_{th} locates the stability limit of such mean-field solution at each γ^*. As for the glassy state, however, α_{gl} proceeds with its γ^*-independent behavior as soon as the density exceeds $\rho_{cr} \simeq 1$ (see Fig. 16(c)). Therefore, similar to what was seen for the case of $L_e = 1.8$, this stripe-shaped region presents LL, MS and RG phases. Noteworthy is that short L_e dramatically reduces the region corresponding to the MS phase, indicating a rapid loss of the configurational degrees of freedom (upon bond stiff-

the laboratory transition is defined to occur when the viscosity reaches 10^4 Poise. Random first order transition (RFOT) theory predicts this to be when the configurational entropy is about $1.0\,k_B$ per particle. To translate our thermodynamic results to the laboratory transition density, we will therefore mean by ρ_G the density where the liquid and glass free energies differ by $1.0\,k_BT$ per particle. Despite the universality of configurational entropy at laboratory transition experimentally confirmed in a wide variety of molecular glasses, this universality must be examined further to see if it is valid in the cytoskeletal system which is an active biological material. Here we just use this fiducial entropy to discuss the qualitative features of our model system.

5. Possible transitions

Visual inspection shows that the phase partition in the upper portion ($\gamma^* > \gamma_c^*$) of $L_e = 1.8$ state diagram exhibits qualitatively identical behavior to that found near the bottom of the stripe-shaped phase region in the diagram of $L_e = 1.2$ case, again indicating that high γ^* and short L_e are comparably competent for making effectively more tense bonds. In this regime, melting from RG via MS region to LL state is expected as ρ is lowered passing ρ_{th} and ρ_{cr} in succession. As for the lower section ($\gamma^* < \gamma_c^*$) of $L_e = 1.8$ diagram, upon increasing density, original homogeneous LL phase becomes destabilized and develops into the proposed ML phase where spatial heterogeneity develops, until finally the RG phase takes the lead. At the crossing point, i.e. $\gamma^* = \gamma_c^*$, RG melts into LL state without going via any intermediate phase. In the case of $L_e = 1.2$, as we go across the phase boundary ρ_{CO} by increasing density, the CO state would transform into the MS phase whereby the distinction between the two types of arrested states with different mechanisms of localization is recovered.

The effective bond stiffness can be varied by manipulating the crosslinking and/or bundling properties or by changing the temperature. Some general features can be extracted from the presented state diagrams, that is high elastic stiffness tends to (1) stabilize the LL state and (2) facilitate the crossover to glassy behavior. The first effect is quite explicit in $L_e = 1.8$ case: as γ^* increases, the elastic-nonlinearity-induced ML phase evolves into LL state with a single stable α_{liq} when $\rho < \rho_{cr}$, whereas purely RG state develops into the MS state when $\rho > \rho_{cr}$. The second effect is clear in $L_e = 1.2$ case; starting either from distinct LL state or from the MS phase, the system would end up with CO behavior as long as γ^* transcends the phase boundary $\gamma_{CO}^*(\rho)$ (inversion of $\rho_{CO}(\gamma^*)$).

Actually the parameter-modulated transformation of the phase behavior in terms of the order parameter α can be directly detected in α_{tagged} versus $\alpha_{neighbor}$ plots,

which explicitly show the emergence and disappearance of, as well as transitions among, various fixed points under the parameter control. In other words, the phase boundaries essentially indicate switching between different fixed point structures of the self-consistent equations. For example, the ρ_{CO} boundary marks the disappearance of the lowest-α fixed point: in LL→CO case, modest discontinuity in α value arises from stability shift to a newly established fixed point in proximity; while a considerable jump in α value is observed in MS→CO case, since no intermediate fixed point develops, the high-α fixed point becomes the only stable attractor. Across the $\gamma_{th}^*(\rho)$ (inversion of $\rho_{th}(\gamma^*)$) boundary from below, the initially bifurcation-generating unstable fixed point becomes stabilized by enhanced stiffness.

In addition to the information obtained from the mechanical stability, the integrated thermodynamic characteristics are more informative of the glassy aspects. In the direction of vitrification, kinetic laboratory glass transition is expected at ρ_G in view of the landscape-dominated transport mechanism triggered at ρ_A and the presence of extensively many possible frozen-in states[33–35]. Whereas the Kauzmann density ρ_K, at which the configurational entropy ceases to be extensive and the glassy configurations are no longer metastable, indicates a thermodynamic transition that ultimately may underlie the kinetic arrest. Though hard to achieve on practical timescale, ρ_K does provide a mean-field estimate of how dense the liquid can be below which a glass transition would be forced to intervene to avoid the entropy crisis[36].

6. Bonded-fraction dependence of mechanical and thermodynamical properties

So far, we have implicitly assumed that all the nearest-neighbor pairs are bonded, i.e. the network is fully connected and there are no free beads at all. In biological fact, however, apart from the fibrous cytoskeletal network, there also exists a colloidal suspension of protein molecules (including detached ABPs, recycled actin monomers, etc.) that contributes equally, if not more, to the crowding interior of a cell, and thus to the excluded volume effect. We mimic such a suspension of molecules simply as a collection of free beads, in which is immersed the nonlinear elastic fiber network which is anchored on the bonded beads. In our mean-field context, the fraction of bonded beads against the free ones is equivalent to the probability for a nearest-neighbor pair to be bonded. We assign an independent parameter $P_b \in (0, 1]$ to indicate this bonded fraction or network connectivity, and assume P_b to be independent of the overall bead density and the effective bond stiffness to purify its influence.

The self-consistent equation to determine α and the expressions of f_{liq} and f_{gl} are modified accordingly:

$$\alpha = \frac{\rho}{6} \int_{1st\,shell} d^3\vec{R}\, g(\rho,R) \left\{ P_b\, Tr\left[\nabla\nabla\beta V_{model}^{eff}(R,\alpha;\beta\gamma,L_e)\right] + (1-P_b)\, Tr\left[\nabla\nabla\beta V_{HS}^{eff}(R,\alpha)\right] \right\}, \quad (14)$$

$$\begin{aligned}
f_{liq} &= P_b\left[\frac{3}{2}\ln\left(\frac{\alpha_{liq}\Lambda^2}{\pi e}\right) - 1\right] + (1-P_b)\left(\ln\rho\Lambda^3 - 1\right) + \int_0^\eta \left(Z_{CS}(\eta') - 1\right)\frac{d\eta'}{\eta'} \\
&+ P_b\,\rho \int_{1st\,shell} d^3\vec{R}\, g(\eta,R)\left[\beta V_{model}^{eff}(R,\alpha_{liq};\beta\gamma,L_e) - \beta V_{HS}^{eff}(R,\alpha_{liq})\right],
\end{aligned} \quad (15)$$

$$\begin{aligned}
f_{gl} &= P_b\,\rho \int_{1st\,shell} d^3\vec{R}\, g(\rho,R)\beta V_{model}^{eff}(R,\alpha_{gl};\beta\gamma,L_e) + (1-P_b)\,\rho \int_{1st\,shell} d^3\vec{R}\, g(\rho,R)\beta V_{HS}^{eff}(R,\alpha_{gl}) \\
&+ \left\{\frac{3}{2}\ln\left(\frac{\alpha_{gl}\Lambda^2}{\pi}\right) - 3\ln\left[erf(\sqrt{\alpha_{gl}}D)\right]\right\} - \delta f.
\end{aligned} \quad (16)$$

In equations for α and f_{gl}, P_b and $(1-P_b)$ lead the effective potential between bonded and non-bonded pairs, respectively; and the influence due to bonded fraction change on the cell constraint term (i.e. the second order term in the effective potential expansion) is contained in the self-consistently determined α_{gl}. As for f_{liq}, the bonded fraction not only modifies the bonding correction to the HS interaction, it also separates the bonded from non-bonded contributions to the entropy cost: for free particles $\ln\rho\Lambda^3 - 1$ should suffice to describe the density dependence of the entropy cost, whereas we use $\frac{3}{2}\ln\left(\alpha_{liq}\Lambda^2/\pi e\right) - 1$ for the bonded beads. Notice the fact that as bonds melt (i.e. P_b decreases), increasing translational symmetry would lower the entropy cost to localize the density waves. We shall show that the logarithmic dependence on α_{liq} used here could at least qualitatively incorporate this feature. Moreover, the bonding entropy due to various choices of bonded pairs among nearest neighbors is not explicitly included, since only the difference between f_{gl} and f_{liq} matters for current purposes. It is easily seen that as $P_b \to 1$ our earlier expressions for a fully connected network (Eqs. (5)(7)(8)) are recovered.

We show in Fig. 17 and Fig. 18 the state diagrams at $P_b = 0.8$ and $P_b = 0.5$ for both typical networks. The corresponding contour maps of α_{liq} and α_{gl} solutions (not shown here) indicate that the behavior of the liquid-like localization strength is not qualitatively affected by changing the bonded fraction, and the glassy solutions are almost quantitatively intact. Yet the transition boundaries are significantly shifted as the bonded fraction varies. For the floppy network (Fig. 17), as P_b decreases, the slower increase of ρ_{th} with γ^* (which implies a lower destabilization density for the liquid-like solution) yields a shrinking MS region and enlarged RG and possibly ML regions. This behavior can be understood as arising from the fact that weaker network connectivity makes the stabilization via "bond trapping" less efficient. In the tense network (Fig. 18), as the bonded fraction drops, both ρ_{th} and ρ_{co} boundaries shift upward
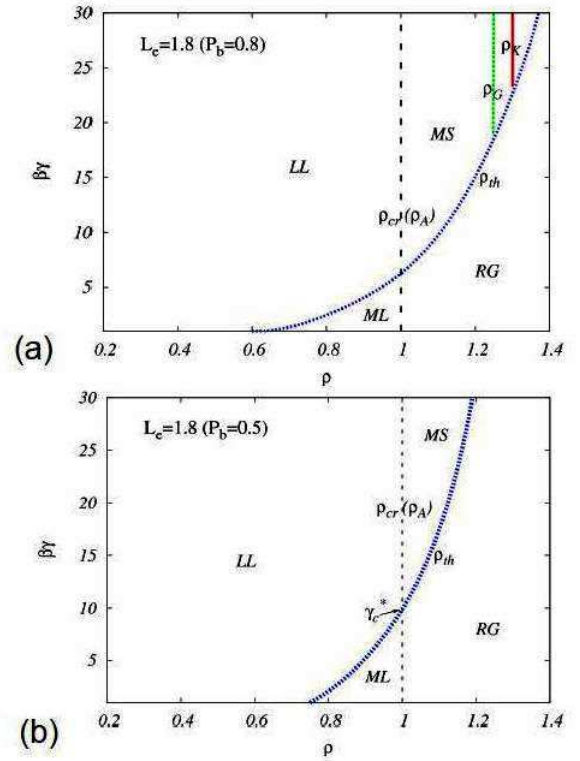
FIG. 17: The state diagrams of a typical floppy network ($L_e = 1.8$) with different bonded fraction. ρ_K (red) and ρ_G (green) are defined as former. (a) $P_b = 0.8$; (b) $P_b = 0.5$: transition densities are absent due to the limited $\beta\gamma$ range shown here.

resulting in an extension of both MS and RG regions into a higher γ^* regime. This observation implies a higher bond stiffness is needed to stabilize the liquid-like solutions so as to trigger the crossover to glassy behavior. As for the dynamical transition density ρ_A (i.e. the critical density ρ_{cr} analyzed in earlier sections), it modestly in-

FIG. 18: The state diagrams of a typical tense network ($L_e = 1.2$) with different bonded fraction. (a) $P_b = 0.8$; (b) $P_b = 0.5$. ρ_G and ρ_K become lower as the bonded fraction decreases.

creases with lowering P_b in the tense network (rises from 0.91 to 0.97 as P_b drops from 1.0 to 0.5) while it remains constant (~ 1) in the floppy network; concomitantly α_A halves its value ($115 \rightarrow 55$) in the tense network while it stays the same (~ 50) for the floppy case.

We next examine the variation in thermodynamics due to the change of bonded fraction. In both networks, ρ_G and ρ_K are found to persist upon decrease in P_b (with the order of $\rho_A < \rho_G < \rho_K$ maintained). In the tense network, ρ_G and ρ_K develop moderate γ^* dependence and shift toward lower density as P_b decreases, as shown in Fig. 18. In the floppy network, ρ_G and ρ_K emerge at considerably higher γ^* as P_b drops indicating greater difficulty in stabilizing LL motion, yet become insensitive to $\beta\gamma$-value thereafter, as seen in Fig. 17(a). When P_b is further lowered to 0.5 (i.e. network being half-connected) transition densities are absent due to the limited range of $\beta\gamma$ shown here (see Fig. 17(b)) and would reappear if we extend $\beta\gamma$ sufficiently.

In contrast, if we use $\ln \rho \Lambda^3 - 1$ for both the bonded and non-bonded contributions to the entropy cost, a dramatic change in ρ_G and ρ_K is found (not shown here): when $P_b = 0.8$, in both networks, ρ_K is barely above ρ_A while ρ_G is entirely skipped; if P_b is further lowered to 0.5, then $f_{liq} > f_{gl}$ for all $\rho \geq \rho_A$ in MS region, indicating a negative configurational entropy which is not

physically meaningful. Actually in our model the highly-localized glassy motion is insensitive to the degree of network connectivity since $\langle \beta V_{model}^{eff}(\alpha_{gl}; \rho > \rho_A; \gamma^*, L_e) \rangle \simeq \langle \beta V_{HS}^{eff}(\alpha_{gl}; \rho > \rho_A) \rangle$ and $\langle \nabla^2 \beta V_{model}^{eff}(\alpha_{gl}; \rho > \rho_A; \gamma^*, L_e) \rangle \simeq \langle \nabla^2 \beta V_{HS}^{eff}(\alpha_{gl}; \rho > \rho_A) \rangle$, thus such a significant drop in transition densities results from an enhanced attractive interaction in the liquid-like phase due to stronger thermal fluctuations (smaller α_{liq}) induced by reduced bond constraints (lower P_b). This energetic enhancement in f_{liq} is balanced, partly, by the decrease in entropic cost (to localize density wave) when $\frac{3}{2} \ln(\alpha_{liq}\Lambda^2/\pi e) - 1$ is used, thereby mitigating the bonded-fraction modulation upon the transition densities, and resulting in a persistent transition possibility over a large P_b range.

In sum, the overall tendencies are clear: decreases in the bonded fraction lower the transition densities ρ_G and ρ_K implying that the system becomes less capable of reconfiguring (or easier to become glassy) upon weakening of the network connectivity; in this sense, the model nonlinear-elastic-bonded interaction encourages liquid-like motion and thereby facilitates more efficient structural rearrangements.

IV. CONCLUSIONS

In this paper, we have modeled the cytoskeleton as an amorphous network of rigidly cross-linked nonlinear-elastic bonds that become tense beyond an intrinsic onset length and buckle otherwise. We study the equilibrium mechanical properties of the model system within the framework established by the self-consistent phonon theory and the free energy functional formulation.

We have obtained an initial understanding of the physical behavior via the calculation of several representative thermodynamic quantities, and by examining the state diagram of typical systems. Diverse mechanical properties of a generic cytoskeleton can be recognized by analyzing the featured phases and possible transitions: the permanent network structure excludes a completely ergodic fluid phase, whereas the nonlinearity in the elastic interaction induces spatial heterogeneity that exhibits through a "martensitic-like" phase with domains of oriented distortions. The probable coexistence of the liquid-like and glassy behavior implies the capability of making structural rearrangements with varying agility in response to mechanical stimuli. The effective bond stiffness tends to stabilize the liquid-like state and facilitates its crossover to glassy behavior, whereas the relative position of the elasticity onset with respect to the nearest-neighbor shell dramatically modulates the transition boundaries; the critical density may no longer mark a sharp transition in certain situations when crossover takes place. In sum, the elasticity onset length determines all possible mechanical phases within a practical parameter range, while the bond stiffness decides which

transitions occur upon the variation of cross-link concentration (thus of the bead density).

We further investigated how the bonded fraction or network connectivity modulates the phase boundaries as well as the thermodynamic terms of the transition densities (ρ_G and ρ_K). We found that decreasing the bonded fraction results in an upward shift of both ρ_{th} and ρ_{CO} boundaries, indicating the need for a higher bond stiffness to compensate for any loss in connectivity, so as to stabilize the liquid-like motion and to trigger its crossover to glassy behavior; on the other hand, the expanded multiple-solution phase region allows for a large stiffness range with extensive configurational degrees of freedom. As for the thermodynamics, the characteristic densities show little dependence on bond stiffness in floppy networks; for tense networks, however, ρ_G and ρ_K become lower upon enhanced bond stiffness, suggesting decreasing configurational degrees of freedom at a certain density as bonds stiffen. Further, for a given density, possible glass transition takes place at a much lower stiffness in tense networks than in floppy ones, while for a certain bond stiffness, the model system becomes vitrified at a lower bead density as more bonds tense up.

As exhibited clearly in the tense network, the logarithmic dependence of the entropy cost (for bonded interaction in the liquid-like phase) on particle localization strength adopted in our free energy functional contains the feature that as more bonds form, the kinetic glass transition would occur at a higher density, suggesting that the nonlinear-elastic-bonded interaction might help resolve local/steric constraints and facilitate escape from topological trapping, resulting in a more dense packing when stuck finally. Fleshing out this conjecture may require coming to term with finite range consideration; we need to go beyond mean-field level and consider activated events among various metastable states (probably via "droplet relaxation" in a mosaic structure[37]). In a biological sense, cells may prefer an interconnected structural skeleton, not only to maintain their architecture, but to realize more efficient structural rearrangements when necessary. As argued by Ingber, the tensed/prestressed hierarchical networks play a central role in producing a well-orchestrated multiscale mechanical response[38].

This work provides a general scheme to study macroscopic mechanical phases in terms of the stability to local mechanical environment, and our current equilibrium model sets up a test field for further incorporated features for a more realistic model, in particular, the motorization effect that makes the system active, far from equilibrium and makes it physically distinct from an ordinary polymer network. It will be interesting to study the interplay of bond constraints and force-environment-sensitive motors in maintaining the cell's architecture and modulating the transition behavior. We also plan to investigate the effect of spatial heterogeneity and visualize the structural rearrangements by combining analytic schemes with simulation techniques.

ACKNOWLEDGEMENTS

[1] J. Howard, *Mechanics of Motor Proteins and the Cytoskeleton*, (Sinauer Assoc., Sunderland, MA, 2001).

[2] K. A. Michie and J. Löwe, Annu. Rev. Biochem. **75**, 467 (2006).

[3] J. Y. Xu, W. H. Schwarz, J. A. Kas, T. P. Stossel, P. A. Janmey, T. D. Pollard, Biophys. J. **74**, 2731 (1998).

[4] T. D. Pollard and G. G. Borisy, Cell, **112**, 453 (2003).

[5] L. A. Cameron, J. R. Robbins, M. J. Footer and J. A. Theriot, Mol. Biol. Cell **15**, 2312 (2004).

[6] S. H. Parekh, O. Chaudhuri, J. A. Theriot and D. A. Fletcher, Nat. Cell Biol. **7**, 1219 (2005).

[7] O. Chaudhuri, S. H. Parekh and D. A. Fletcher, Nature **445**, 295 (2007).

[8] A. Weeds, Nature **296**, 811 (1982).

[9] C. C. Cunningham, J. B. Gorlin, D. J. Kwiatkowski, J. H. Hartwig, P. A. Janmey, H. R. Byers, and T. P. Stossel, Science **255**, 325 (1992).

[10] P. A. Janmey, Curr. Opin. Cell Biol. **2**, 4 (1991).

[11] D. H. Boal, *Mechanics of the Cell* (Cambridge University Press, New York, 2002).

[12] A. R. Bausch and K. Kroy, Nature Phys. **2**, 231 (2006).

[13] P. A. Janmey, M. E. McCormick, S. Rammensee, J. L. Leight, P. C. Georges and F. C. MacKintosh, Nat. Mater. **6**, 48 (2007).

[14] K. D. Costa, W. J. Hucker and F.-P. Yin, Cell Motil. Cytoskelet. **52**, 266 (2002).

[15] P. M. Bendix, G. H. Koenderink, D. Cuvelier, Z. Dogic, B. N. Koeleman, W. M. Brieher, C. M. Field, L. Mahadevan and D. A. Weitz, Biophys. J. **94**, 3126 (2008).

[16] B. Fabry, G. N. Maksym, J. P. Butler, M. Glogauer, D. Navajas, and J. J. Fredberg, Phys. Rev. Lett. **87**, 148102 (2001).

[17] S. J. Gunst and J. J. Fredberg, J. Appl. Physiol. **95**, 413 (2003).

[18] M. L. Gardel, J. H. Shin, F. C. MacKintosh, L. Mahadevan, P. Matsudaira and D. A. Weitz, Science **304**, 1301 (2004).

[19] X. Trepat, L. Deng, S. S. An, D. Navajas, D. J. Tschumperlin, W. T. Gerthoffer, J. P. Butler and J. J. Fredberg, Nature **447**, 592 (2007).

[20] E. H. Zhou, X. Trepat, C. Y. Park, G. Lenormand, M. N. Oliver, S. M. Mijailovich, C. Hardin, D. A. Weitz, J. P. Butler and J. J. Fredberg, Proc. Natl. Acad. Sci. USA **106**, 10632 (2009).

[21] E. M. Huisman, T. van Dillen, P. R. Onck and E. Van der Giessen, Phys. Rev. Lett. **99**, 208103 (2007).

[22] T. Shen and P. G. Wolynes, New J. Phys. **8**, 273 (2006).

[23] G. H. Koenderink, Z. Dogic, F. Nakamura, P. M. Bendix,

F. C. MacKintosh, J. H. Hartwig, T. P. Stossel and D. A. Weitz, Proc. Natl. Acad. Sci. USA **106**, 15192 (2009).

[24] G. Lenormand and J. J. Fredberg, Biorheology **43**, 1 (2006).

[25] L. Verlet and J. -J. Weis, Phys. Rev. A **5**, 939 (1972).

[26] M. Fixman, J. Chem. Phys. **51**, 3270 (1969).

[27] R. W. Hall and P. G. Wolynes, Phys. Rev. Lett. **90**, 085505 (2003).

[28] T. Shen and P. G. Wolynes, Phys. Rev. E **72**, 041927 (2005).

[29] J. D. Stevenson, A. M. Walczak, R. W. Hall, and P. G. Wolynes, J. Chem. Phys. **129**, 194505 (2008).

[30] Y. Singh, J. P. Stoessel and P. G. Wolynes, Phys. Rev. Lett. **54**, 1059 (1985).

[31] R. W. Hall and P. G. Wolynes, J. Phys. Chem. B **112**, 301 (2008).

[32] E. Zaccarelli and W. C. K. Poon, Proc. Natl. Acad. Sci. USA **106**, 15203 (2009).

[33] T. R. Kirkpatrick and P. G. Wolynes, Phys. Rev. A **35**, 3072 (1987).

[34] T. R. Kirkpatrick and D. Thirumalai, Phys. Rev. Lett. **58**, 2091 (1987).

[35] T. R. Kirkpatrick and P. G. Wolynes, Phys. Rev. B **36**, 8552 (1987).

[36] W. Kauzmann, Chem. Rev. **43**, 219 (1948).

[37] M. Dzero, J. Schmalian and P. G. Wolynes, Phys. Rev. B **72**, 100201 (2005).

[38] D. E. Ingber, FASEB J. **20**, 811 (2006).